thesis title

Pruthvi Mehta

2021

Contents

Chapter 1

Introduction

Chapter 2

The Super Kamiokande Detector

2.1 The Super-Kamiokande detector

2.1.1 Background and detector design

Super-Kamiokande is a neutrino observatory consisting of a cyclindrical tank which is 41.4 m in height and 39.3 m in diamter, and filled with 50kton of ultrapure water and gadolinium sulphate. It is used as a neutrino detctor for atmospheric, solar and astrophysical neutrinos, as well as being a far detector of the Tokai-to-Kamioka neutrino beam. It is based in the Mozumi mine, located in Gifu Prefecture, Japan. Due to it's location being underneath Mount Ikenoyama, 1000m underground, it is shielded as much as possible from the cosmic ray muon detector background. Super-Kamiokande is divided into two concentric cylinder volumes, consisting of the inner detector (ID) and outer detector (OD) using a stainless steel structure which supports the photomultiplier tubes. Tyvek and black polyethylene terephthelate sheets are mounted on this structure in order to optically seperate the inner and outer detector [**suzukiSuperKamiokandeExperiment2019**].

The inner detector is a cylinder which has a diameter of 33.8 m and a height of 36.2m, and has a fiducial volume of 22.5ktons of water. It is host to 11,129 photomultiplier tubes which give 40% photocoverage of its inner surface, with the specific photomultiplier model chosen being the hemispherical, 50.8 cm diameter Hamamastu R3600 model. The outer detector has only 1885 photomultiplier tubes which are mounted on the outside of stainless steel structure, each with a smaller diameter of 20cm, and are either the R1408 or R5912 Hamamatsu model. Each outer detector photomultiplier tube is attached to a 50cm x 50cm wavelength shifting plate, improving the light collection ability in the OD [**fukudaSuperKamiokandeDetector2003**].

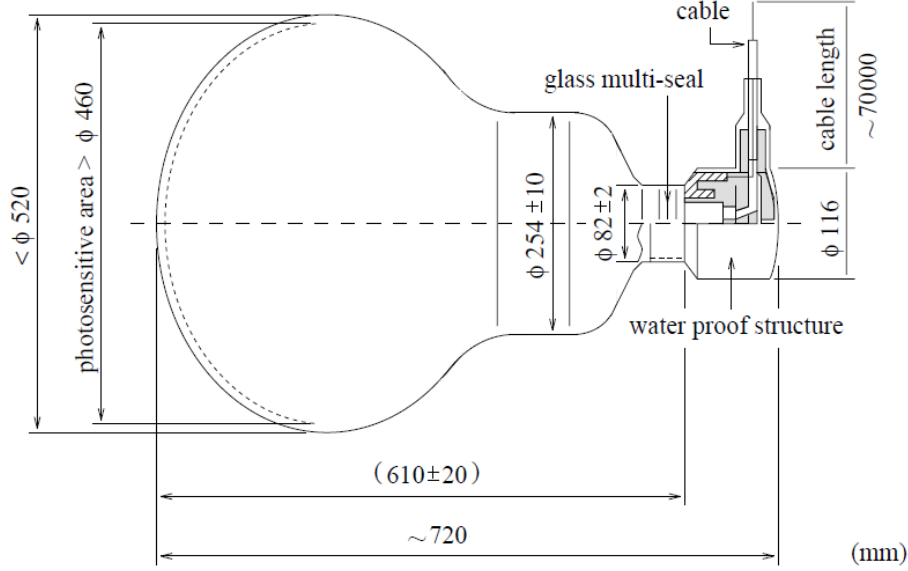A detailed schematic of the photomultiplier tubes used in Super-Kamiokande

Figure 2.1: Schematic of an ID 50 cm Super-Kamiokande PMT [**fukudaSuperKamiokandeDetector2003**].

can be seen in Figure **??**. The photocathodes used in these PMTs are comprised of bialkali antimony-potassium-caesium material (Sb-K-Cs), which give a greater sensitivity on to longer wavelengths, giving the greatest spectral response at 360 nm, near the ultraviolet section. This makes these types of photocathodes suitable to use for matching with light sources in the blue region of the visible spectrum, which is the region in which the wavelength of Cherenko photons lie. The 11 dynodes which are inside the photomultiplier tube are arranged in a "venetian blind" fashion, meaning that the dynodes consist of an assembly of parallel strips. This results in a good collection efficiency of the multiplied electrons and gives decent protection from external magentic fields. More protection from external magnetic fields is provided by a set of Helmholtz coils which are aligned around the inner walls of the innter detector, which reduce the ambient background geomagnetic field from 450mG to 50mG. This is needed due to the systematic bias that could occur due to the strength and uniform direction of the geomagnetic field affecting the photon trajectories and consequently the photomultiplier tube hit timing.

Radioactivity from radon, uranium and thorium radioisotopes in the Super-Kamiokande tank water and radon in the surrounding air could provide a low energy background to measurements which should be negated. In low-energy analyses, such as the analysis in this thesis, this becomes an even more significant issue. Microbes present in the mine water also present a problem as they cause a reduction in the value of the light attenuation length by a factor of e.

Therefore the water used in Super-Kamiokande has to undergo a purification process - the water used is continously reprocessed at a rate of 30 tons h^-1 in a closed loop system, which is the same method used to purify the water when refilling the tank. The first step of this water purification process is to use a 1µm mesh filter to remove large particulates of impurities from the water. [**fernandezmenendezNeutrinoPhysicsPresent2018**].A heat exchanger is then used to cool down the water to a constant 13.0 °C to reduce the dark noise hits of the photomultiplier tubes and the growth of the microbes. A treatment with ultraviolet light is then used to kill any remaining microbes in the water. Radon-free air is then dissolved into the water to aid in the later process of radon removal from the water and a high performance membrane ultra filter (UF) is used to remove organic compounds about 10 nm in diamater from the water. After this step a membrane degasifier removes the dissolved radon, where 30 L of radon reduced air is supplied to the membrane degasifier. The dissolved radon will transfer across the membrane but the water will not, allowing for efficient radon reduction. The inner detector tank water is circulated by injecting the water at the bottom of the tank and exctracting it from the top, where the convection currents are able to maintain the temperature in the region within 11m to the bottom of tank, however, outside this region the present temperature gradient causes an asymmetry in the attenuation of light, which is discussed more in Chapter 3.

An air purification system is also installed in Super-Kamiokande in order to reduce the amount of Radon present which could dissolve into the tank and affect measurements. The level of radon activity achieved after this air purification has taken place is 1 mBq/m^3.

The Super-Kamiokande experiment began taking data on 1st April 1996, and due to maintenance was shut down in July 2001, which was phase I of the experiment. A table of the Super-Kamiokande phases is shown in Table **??**. During the refilling of the tank after maintenence, there was cascade of PMT implosions that occurred on the 12th of November 2001, which were triggered by the implosion of a single photomultiplier tube, due to a microfracture in the neck of the tube. This implosion destroyed about 7,000 of the PMTs and in order to avoid such chain reactions in the future, from 2002 onwards all of the inner detector PMTs were fitted with acrylic covers and fiber-glass reinforced plastic (FRP) cases. The experiment resumed in October 2002, and phase II of Super-Kamiokande began, and by October 2005 the experiement was fully rebuilt and resumed data taking with the full number of photomultiplier tubes in July 2006 which marked the beginning of Super-Kamiokande phase III. Super-Kamiokande phase IV began in September 2008 where a new data aquisition system and charge to time (QTC) based electronics with Ethernet (QBEE) was deployed in order to measure arrival times and integrated charge for inner detector and outer detector photomultiplier tube signals. This replaced the ATM (Analogue and Timing Module) which was used in Phase I, II and III of Super-Kamiokande. The improvements in electronics and calibration methods meant that when Super-Kamiokande phase IV started running in September of 2008, electrons with energies as low as 3.5 MeV were able to be detected.

[**fernandezmenendezNeutrinoPhysicsPresent2018**].

Phase	Phase Period	Total PMT number		FRP case?	Electronic type
		ID (Coverage)	OD		
SK-I	Apr. 1996 - Jul. 2001	11146(40%)	1884	no	ATM
SK-II	Oct. 2002 - Oct. 2005	5182(19%)	1884	yes	ATM
SK-III	Jul. 2006 - Sep. 2008	11129(40%)	1884	yes	ATM
SK-IV	Sep. 2008 - Today	11129(40%)	1884	yes	QBEE
SK-V		11129(40%)	1884	yes	QBEE

Table 2.1: Phases of Super-Kamiokande and main properties of each phase

2.1.2 Data aquisition system

As shown in Table **??**, Phase IV of the experiment marked the beginning of
Super-Kamiokande using QTC-based Electronics with Ethernet (QBEEs). Each
QBEE board used in Super-Kamiokande contains 24 photomultiplier tube in-
put channel, where each channel uses a charge-to-time (QTC) converter and a
time-to-digital converter placed in series as shown in Figure **??**. After a single
photoelectron is produced by the photomultiplier tubes after incident photons
have been recieved upon it, the dynodes inside the photomultiplier tube am-
plify this photoelectron so that each photoelectron that strikes the surface of
the dynode produces several more photoelectrons, which is outputted from the
the dynodes as an analogue signal. This signal then enters a charge-to-time
converter (QTC), an application specific integrated circuit (ASIC) which was
specifically designed for Super-Kamiokande in order to detect photomultiplier
tube signals using built-in discriminators and to produce output timing signals
whose widths represent the integrated charge of the PMT signal. The QTC used
has three input channels per chip, which has three gain ranges (Small, Medium,
Large as shown in Figure **??**). There is a built in discriminator inside the QTC
which determines whether the the signal from a PMT is a "hit". If the PMT
signal exceeds the threshold value of this discriminator, the QTC integrates the
charge of the signal over the next 400ns, and a square wave pulse is generated
whose pulse width is proportional to the intergrated charge of the input signal
from the PMT. The next 400ns is used to discharge the integrated charge from
the QTC, leading to a total channel dead time of 900 ns due to summing the
charge integration and discharge of the QTC.

A time-to-digital converter (TDC) then digitises the output time signal, so
the PMT charge information is retained. These digitised outputs are collated
by 20 front-end computers which collects all the information from the inner
and outer detectors, with each computer taking the PMT hit information from
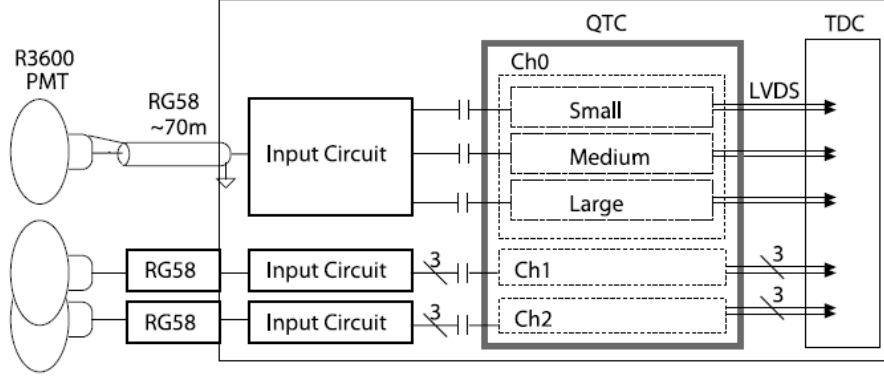30 inner detector and 20 outer detector QBEE boards and sorting the PMT

Figure 2.2: Schematic of the charge-to-time converter circuit [**nishinoHighspeedChargetotimeConverter2009a**].

hit time information in order of the raw hit time. This information is then sent to "merger" computers, who then produce a full time-ordered list of all PMT hits. These merger computers then apply software triggers to select event candidates, using N_{200}, a quantity which determines the number of PMT hits in a 200 ns timing window. When the value of N_{200} surpasses the threshold value of a certain trigger type (whether it is a SLE (Super Low Energy), LE (Low Energy), HE (High Energy), SHE (Super High Energy), OD (Outer Detector) or AFT (After Window) trigger), the trigger is used to select an event candidate. The SLE, LE, HE and SHE triggers roughly define the energy of a certain event, based on the number of hits detected. The OD trigger is used to veto events, and the AFT trigger is of special importance to the analysis in this thesis: it is used to discern when a neutron is produced after a neutrino interaction. Another set of computer acts as an "organiser": it takes all the information regarding the event candidates from the "merger" computers and writes them onto disks [**fukudaSuperKamiokandeDetector2003**].

2.2 Event Reconstruction

2.2.1 Vertex Reconstruction

For low energy events (events up to 100MeV), Super-Kamiokande currently uses BONSAI (Branch Optimisation Navigating Successive Annealing Interactions) for event reconstruction. Vertex reconstruction for Super-Kamiokande has undergone changes and improvements depending on the phase of the experiment. For Phase I of Super-Kamiokande, vertex reconstruction depended on a lattice of test vertices with 4m spacing throughout the detector, with a specific measure of goodness for each test vertex: the test vertex with the highest measure of goodness would have around it a more finely spaced grid, and the process would

be repeated. For Phase II of Super-Kamiokande due to the reduced number of PMTs, this approach was no longer as successful as it was in Phase I and as a result the reconstruction perfomance declined, and BONSAI was created as a replacement. Instead of using a fixed grid which was the case with SK-I and SK-II, BONSAI creates test vertices by selecting groups of four PMT hits and seeing where the timing residuals of the PMT hits would be most reduced. After these test vertices have been indentified, a maximum likelihood fit over all the PMT hits in the event is performed, shown in Equation **??**.

$$\mathcal{L}(\vec{x}, t_0) = \sum_{i=1}^{N_{\mathrm{hlt}}} \log(P(t - t_{\mathrm{tof}} - t_0)) \tag{2.1}$$

where $(\vec{x}, t_0)$ is the test vertex, and $(P(t - t_{\mathrm{tof}} - t_0))$ is the probablility density function of the timing residual, which for each PMT hit is defined as $(t - t_{\mathrm{tof}} - t_0)$, where t_0 is the time of the interaction, t_{tof} is the time of flight from the interaction vertex position to the position of the hit PMT, t is the PMT hit time. The vertex resolution

2.2.2 Direction Reconstruction

Cherenkov light is emitted in a conical formation as electrons and positrons travel through water, with a Cherenkov angle of $\approx 42°$. BONSAI can reconstruct the direction of these particles by using this information along with the reconstructed vertex. This reconstruction occurs using a maximum likelihood function defined in Equation **??**.

$$\mathcal{L}(\vec{d}) = \sum_{i}^{N_{20}} \log(f(\cos\theta_i, E)) \times \frac{\cos\theta_i}{a(\theta_i)} \tag{2.2}$$

$f(\cos\theta_i, E)$ is the expected distribution of the angle between the vector of the direction $\vec{d}$ of the particle, and the observed Cherenkov photon from the position of the reconstructed vertex. The reason there is a spread in this energy distribution is because while the highest value of this distribution occurs at the cosine of the opening Cherenkov angle of 42°, due to the particle travelling through the water being Coulomb scattered multiple times, there is a variation in the angle because of the varying particle energy. N_{20} is the number of hits whose residual hit time is within 20ns of the time of the reconstructed event, which is used in order to reduce the amount dark noise and scattered photons contribute to the direction reconstruction calculation. The variable $a(\theta_i)$ is used in the second term in Equation **??**, and it is linked to the angle of incidence of the photon on the PMT $a(\theta_i)$, and is a correction factor stemming from the acceptance of PMTs and therefore linked to the shape of the PMT and it's acrylic case.
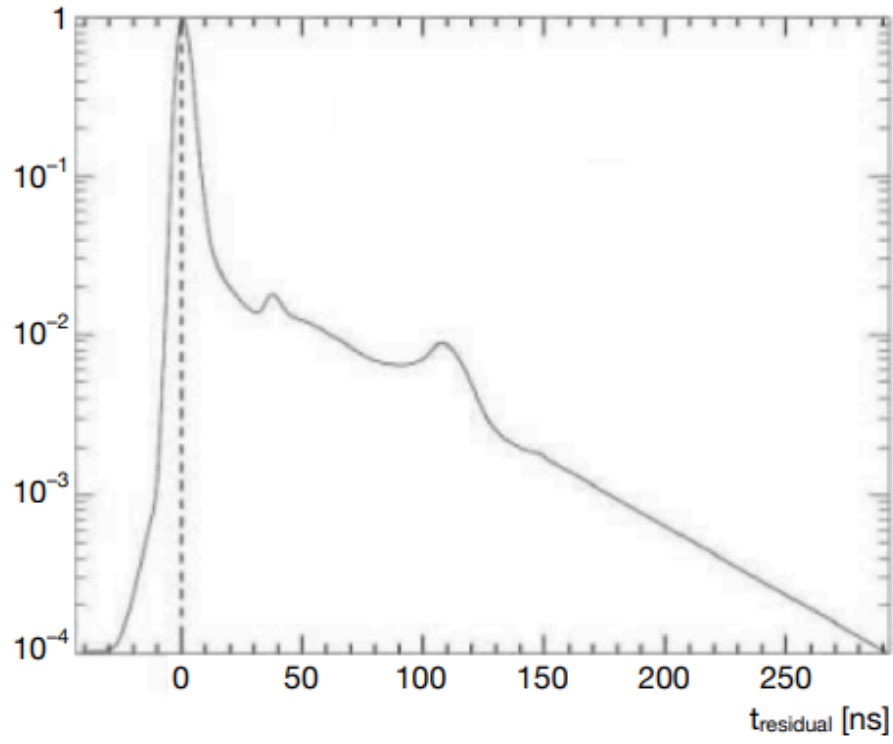
Figure 2.3: Probability density of the timing residual $P(t - t_{\text{tof}} - t_0)$, where t_0 use for the vertex reconstruction maximum likelihood fit. The peaks at 30ns and 100ns are caused by PMT after-pulsing. Figure from [.]
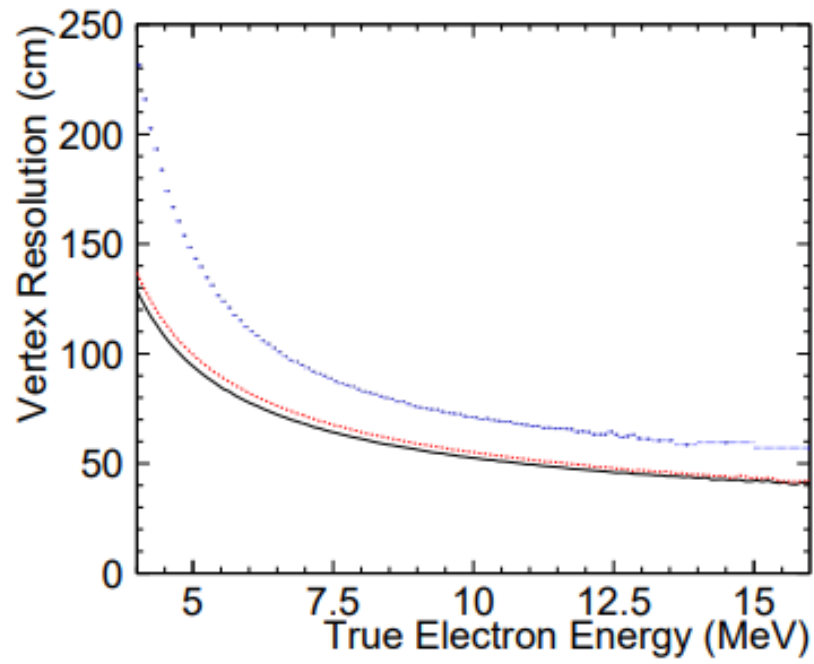
Figure 2.4: The vertex resolution (the point at which 68% of the events in the distance distribution between the actual and reconstructed vertex are contained) for the different SK phases. SK-I (Blue), SK-III (Red), SK-IV (Black). Figure from [.]

2.2.3 Energy reconstruction

The kinetic energy of a particle is proprtional to the amount of Cherenkov photons emitted from it, and if we assume that the Cherenkov photons in a single event come from a single electron, we can reconstruct the total energy of the electron. Instead of using the number of photoelectrons of all hit photomultiplier tubes to reconstruct the energy of low energy events, the number of hit photomultiplier tubes is used instead. The reasons for this are threefold - firstly, low energy events emit a small number of Cherenkov photons, and therefore average about one photon per hit PMT. Secondly, at single photoelectron level, the resolution of photoelectrons is bad, and third, the number of photoelectrons produced is related to the gain of the photomultiplier tubes, which is given by equation:

$$G(i) \propto \frac{Q_{obs}(i)}{N_{obs}(i)} \tag{2.3}$$

where $G(i)$ is the gain of each PMT and $Q_{obs}(i)$ is the average charge for each inner detector photomultiplier tube, and $N_{obs}(i)$ is the number of times that photomultiplier tube i registers a charge which is greater than the threshold charge value. Due to the variation in gain value not affecting the number of hit photomultiplier tubes as much as it does for the number of photoelectrons, number of hit PMTs is used instead. Energy reconstruction uses N_{50}, which is the number of photomultiplier tube hits in a 50 ns window, which allows for the rejection of dark noise hits for the photomultiplier tubes. The number of effective photomultiplier tubes which are hit, the number of hit PMTs in this timing window of 50ns is summed up, while being weighted with correction factors, shown in Equation **??** [**uenoAnalysisNuclearDeexcitationa**].

$$N_{eff} = \sum_{i=1}^{N_{50}} \left[(X_i - \epsilon_{\text{dark}} + \epsilon_{\text{tail}}) \times \frac{N_{\text{all}}}{N_{\text{alive}}} \times \frac{1}{S(\theta_i, \phi_i)} \times \exp\left(\frac{r_i}{\lambda}\right) \times G(i) \right] \tag{2.4}$$

where X_i is the correction factor hits with many photoelectrons. This correction factor is important because if some photomultiplier tubes are hit by multiple photons (for example, if the edge of the fiducial volume is where the event vertex took place). The number of photoelectrons produced by each hit photomultiplier tube is estimated using the occupancy of the eight photomultiplier tubes which surround it. Using the number of hit photomultiplier tubes (n_i) and the number of functional photomultiplier tubes that surround the i-th photomultiplier tube (N_i), the formula for X_i is shown in Equation **??**.

$$X_i = \begin{cases} \log\left(1 - n_i/N_i\right)^{-N_i/n_i} & (n_i < N_i) \\ 3 & (n_i = N_i) \end{cases} \tag{2.5}$$

ϵ_{dark} in Equation **??** is a correction factor for dark noise hits, shown in Equation **??**, where R_{dark} is the average value for the dark rate during the run

period that the event is in and N_{PMTalive} is the number of active photomultiplier tubes in the inner detector.

$$\epsilon_{\mathrm{dark}} = \frac{N_{\mathrm{PMTalive}} \times R_{\mathrm{dark}} \times 50 \text{ ns}}{N_{50}} \tag{2.6}$$

ϵ_{tail} is the correction factor for photomultiplier tube hits which are in the tail end of the 50ns timing window, and is defined in Equation **??**.

$$\epsilon_{\mathrm{tail}} = \frac{N_{100} - N_{50} - N_{\mathrm{alive}} \times R_{\mathrm{dark}} \times (100 - 50)\mathrm{ns}}{N_{50}} \tag{2.7}$$

$\frac{1}{S(\theta_i,\phi_i)}$ is the inverse of the effective area of the ith hit photomultiplier tube photocathode, from the direction of the incident photon given by (θ_i, ϕ_i).

$G(i)$ is the gain correction for the quantum efficiency of the photomultiplier tubes and $exp(\frac{r_s}{\lambda})$ is the correction for water transparency which accounts for the amount of attenuation undergone by the photons in water, where λ is the water transparency measured during the run period which includes the event, and r_i is the distance between the reconstructed event vertex and the i-th hit PMT.

The average of each N_{eff} distribution is taken, after producing multiple N_{eff} distributions with fixed energies using Monte Carlo. These energies are fitted with a polynomial which is a function of the averaged N_{eff} distribution, so the reconstructed energy is converted from N_{eff}.

Chapter 3

Super-Kamiokande Detector Calibration

Chapter 4

The UK Light Injection System

Chapter 5

Super-Kamiokande Gadolinium Upgrade

5.1 Physics motivation behind Super-Kamiokande Gadolinium Upgrade

In order to be able to possibly observe the supernova relic neutrino (SRN) flux, also known as diffuse supernova neutrino background (DSNB) flux it was proposed that Gadolinium (Gd) should be added to the the water in Super-Kamiokande. Natural isotopes of gadolinium have large thermal neutron capture cross sections. As a result of this, when neutrons are captured on them there is a cascade of gamma rays that occurs, with an energy totalling 8 MeV, whereas neutron capture that occurs on hydrogen produces a single 2.2 MeV gamma ray. Two such natural isotopes, Gd-155 and Gd-157 have thermal neutron capture cross sections of 60740 barns and 253700 barns respectively, while the thermal neutron capture cross section of hydrogen is just 0.329 barns [**meoMeasurementNeutronCapture**]. The Super-Kamiokande with Gadolinium experiment, formerly known as GADZOOKS! (Gadolinium Antineutrino Detector Zealously Outperforming Old Kamiokande, Super!) was proposed in 2003, which stated the intention of enriching Water Cherenkov detectors with water soluble gadolinium salt. The ultimate aim is to load a total amount of gadolinium in the form of gadolinium sulphate octahydrate(

$$\mathrm{Gd_2\left(SO_4\right)_3 \cdot 8H_2O}$$
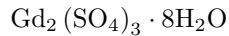
) in Super-Kamiokande which equates to 0.2% of Gd by mass, which would allow for 90% neutron capture efficiency. The ability to tag neutrons efficiently in Super-Kamiokande will benefit multiple physics topics, not only for the aforementioned observation of SRN flux, but also for analyses involving atmospheric neutrinos and proton decay.

A massive amount of energy is relased when a core-collapse supernova (SN) occurs, about 10^{46} J. The vast majority of this energy (99%) is released in the form of neutrinos, and due to neutrinos interacting with matter only very weakly, these traverse space with barely any attenuation. The interaction through which neutrino detectors such as Super-Kamiokande detect SRN flux is through inverse beta decay (IBD), shown in Equation **??**.

$$\bar{\nu}_e + p \rightarrow n + e^+ \tag{5.1}$$

Due to the large cross section of the interaction, these events constitute about 88% of the total number of events in the detector [**martiEvaluationGadoliniumAction2020**]. With efficient neutron tagging in Super-Kamiokande, the backgrounds (charged current interactions and muon spallation) in the search for SRN flux neutrinos would be largely reduced. The neutral current quasielastic (NCQE) background would still remain due to the way the gamma rays arising from neutron capture mimic the signal of the inverse beta decay (IBD) reactions: a schematic of both NCQE and IBD reactions are shown in Figure **??**. The measurement of the NCQE interactions using T2K beam flux can aid in understanding this background more due to the T2K flux peak being near the atmospheric neutrino flux peak (600 MeV).
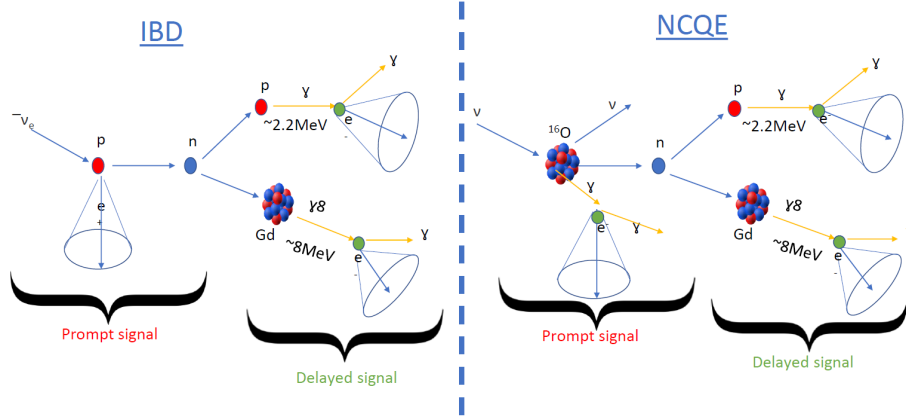

Figure 5.1: Schematic showing the IBD and NCQE interaction mechanisms

Efficient neutron tagging aids information about neutrino energy and neutrino interaction type, and when it comes to studying atmospheric neutrino oscillations, accurate neutrino energy reconstruction is particularly important. Figure **??** shows the fraction of non-visible energy as a function of the number of tagged neutrons from simulations of atmospheric neutrino interactions at Super-Kamiokande. Here E_ν is the energy of the atmospheric neutrino and E_{vis} is the energy that is reconstructed from charged particles. Due to these neutrinos interacting with nuclei in the detector, more neutrons are produced,

and with efficient neutron tagging on gadolinium the neutrino energy can be properly reconstructed.
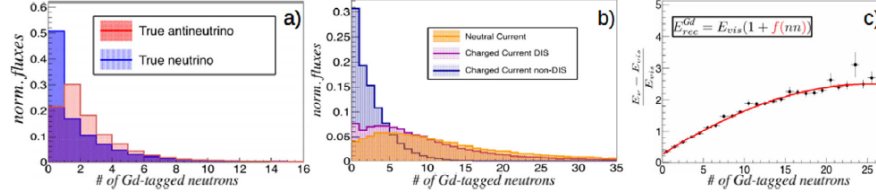

Figure 5.2: MC study of (a) neutron multiplicity production for ν and $\bar{\nu}$, (b) neutral current, charged current and deep and non-deep inelastic scattering, (c) the correction to the visible energy as a function of neutrino multiplicity. Taken from [**martiEvaluationGadoliniumAction2020**].

Proton decay searches benefit from the addition of gadolinium to Super-Kamiokande because the main background to proton decay analyses come from atmospheric neutrino interactions, due to Figure **??** showing that atmospheric neutrinos cause at least one neutron to be produced.

5.2   The EGADS project

In 2009, prior to the additon of gadolinium in Super-Kamiokande, the EGADS (Evaluating Gadolinium's Action on Detector Systems) project was used to evaluate how the inclusion of gadolinium sulphate octahydrate would affect water quality and detector components inside Super-Kamiokande and their analyses. It was also used to observe how to reduce the visible neutron background from spallation and neutrons from fission chains from the uranium and thorium impurities in the gadolonium sulphate. EGADS is a cylindrical 200 ton stainless steel tank in a cavern near Super-Kamiokande and has its own water purification system and gadolinium sulphate octahydrate dissolving system.

Observing the impact the addition of gadolinium sulphate octahydrate had on the water quality and components was especially crucial, and after loading 0.2% gadolinium sulphate into the the EGADS tank in 2013, 240 PMTs were installed into the detector. 224 of these are the 50 cm Super-Kamiokande inner detector PMTs, with 60 of these having the same FRP and acrylic covers as the inner detector PMTs. Much like Super-Kamiokande, the active photocoverage for EGADS is 40%, with the inside walls of the detector also being covered in black polyethylene terephthalate sheets. However, unlike Super-Kamiokande, there is no outer detector in EGADS. Figure **??** shows the PMT map for the EGADS detector along with the PMT types. Along with the PMTs which are identical to the ones inside Super-Kamiokande, EGADS also contains PMTs which are used for research and developement for use inside Hyper-Kamiokande [**martiEvaluationGadoliniumAction2020a**].
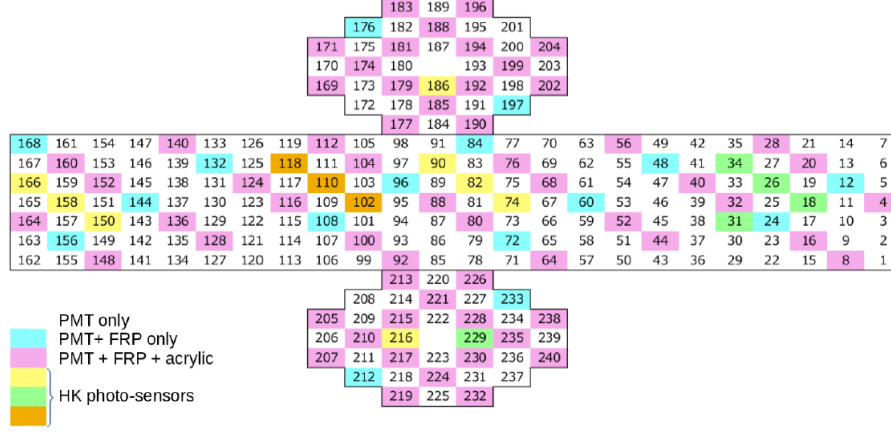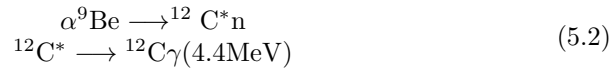
Figure 5.3: Map of unrolled cylindrical EGADS detector with PMT types. Taken from [**martiEvaluationGadoliniumAction2020a**].

Measurements regarding neutron tagging were also taken using an Americium/Beryllium (Am/Be) source placed inside EGADS. Using an Am/Be neutron source to observe gadolinium's efficacy with respect to tagging neutrons is feasible because the Am/Be source decays as in Equation **??**. It produces a prompt 4.4 MeV gamma ray alongside a neutron during it's decay process, and as a result the prompt 4.4 MeV signal can serve as a trigger signal, while the following hundreds of microseconds can be used as a timing window within which to scan for the neutron. Due to its similarity to the neutral current quasieleastic events studied in the analysis in this thesis, it can serve as a helpful control sample and is used in the calculation of the detector response uncertainty in Chapter 7.

$$
\begin{aligned}
\alpha\,^9\mathrm{Be} &\longrightarrow\,^{12}\mathrm{C}^*\mathrm{n} \\
^{12}\mathrm{C}^* &\longrightarrow\,^{12}\mathrm{C}\gamma(4.4\mathrm{MeV})
\end{aligned}
\tag{5.2}
$$

The delayed neutron capture time from an Am/Be source used in EGADS with the gadolinium sulphate concentration of 0.2% is shown in Figure **??**. Here, we can see that the neutron capture time from the data is 29±0.3 μs and for the Monte Carlo it is 30±0.8 μs.
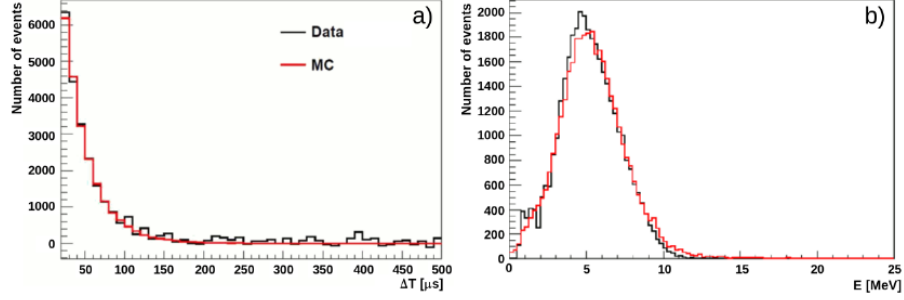
18

Figure 5.4: a) Delayed neutron capture time from prompt event with Am/Be source. (b) Reconstructed energy from gamma rays after neutron capture.

EGADS water transparency and and gadolinium sulphate concentration was monitored daily to ensure similarity to ensure no negative effects to the detector components. Figure **??** shows the transparency and concentration from bottom, top and centre sampling ports in EGADS, with the blue band being typical water transparency values for Super-Kamiokande. It shows that the water transparency values remain comparable to Super-Kamiokande values and that there is very little variation from the final target gadolinium sulphate concentration, as there is little variation from the black dashed line.
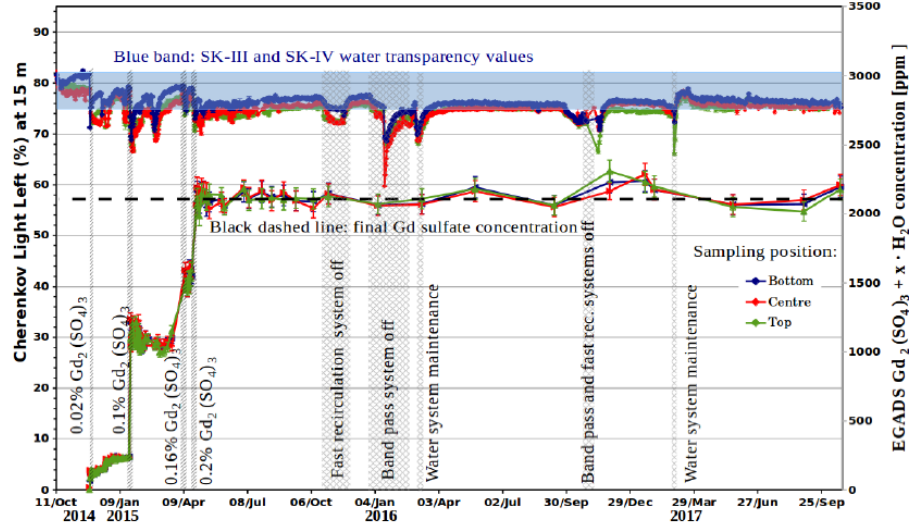

Figure 5.5: The upper lines are Cherenkov light left (%) and the lower three lines represent gadolinium sulphate concentration. The blue, red and green lines represent measurements taken from the bottom, centre and top sampling ports, respectively. Taken from [**martiEvaluationGadoliniumAction2020a**]

19

EGADS also represented the most realistic possible soak test, and after two and a half years of running EGADS was emptied in November 2017 to check the condition of the inner structure and the photomultiplier tubes. There was no deteriation of any of the components, which was an excellent sign for a detector designed to so closely resemble the conditions for the Super-Kamiokande Gadolinium upgrade.

5.3 Gadolinium loading into Super-Kamiokande

After the success of EGADS, the Super-Kamiokande Gadolinium project was formed in 2015 when the final goal of adding 0.2% gadolinium sulphate octahydrate by mass to the detector. 10% of the target concentration was then loaded into Super-Kamiokande from July 14th to August 17th 2020. The details of the various aspects of the gadolinium loading are mentioned in the next subsections: the SK-Gd water system, the flow of the water in the detector, and the loading of the gadolinium sulphate octahydrate powder.

The SK-Gd water system

The SK-Gd water system was designed to dissolve gadolinium sulphate octahydrate into the detector water, pass it through a "pretreatement" system to remove contaminants from the water, and then to continously circulate it. Figure **??** shows a schematic of the system. The

$$Gd_2 \left(SO_4\right)_3 \cdot 8H_2O$$
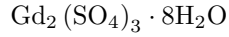
powder is transported to a weighing hopper whch dissolves it into water held in a dissolving tank, which allows for exact amounts of the powder to be dissolved to attain the specific concentration required. The water in Super-Kamiokande is fed into a solvent tank, and then to the dissolving tank, from which it recieves the gadolinium sulphate octahydrate from the shear blender. Water from this dissolving tank mixes the powder, and this combination is sent to the pretreatment system. The design for this treatment system was successfully tested in EGADS and involves treating this solution with ultraviolet light. Positively charged impurites dissolved in the solution (such as radium ions) and negatively charged impurities (such as uranium) are removed using a cation and anion exchange resins respectively. The gadolinium loaded water is next transferred to a UV steriliser to remove bacteria introduced during the dissolving process. This pretreatement process only occurs during gadolinum octahydrate sulphate dissolution, and not during the recirculation process. The recirculation process is similar to the pretreatement process, but with ultrafiltration modules installed in the final stage, and heat exchmage units used before the water is returned to the detector, to help maintain exact control over the water temperature.
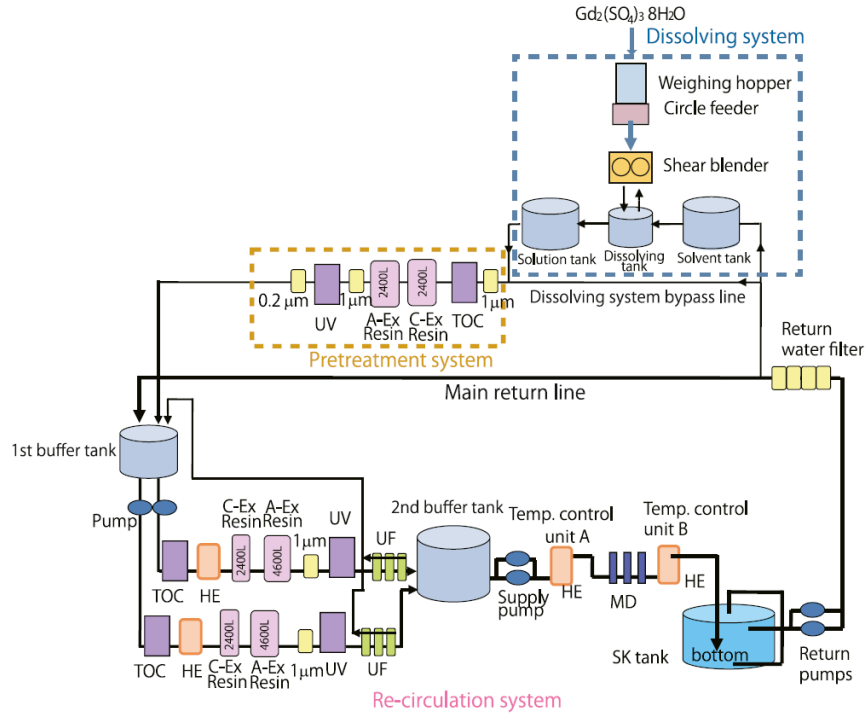
Figure 5.6: Schematic of the SK-Gd water system

Control of water parameters in SK-Gd

Before gadolinium loading occurred, the water temperature in the tank was set at 13.9 °C exactly and was circulated at this temperature for about 45 days. The temperature of the "supply water" (water sent from the water system to the detector tank) was set to a lower temperature (13.55 °C) as Gd-loading began. This gradient in the density between the tank water and supply water meant that spatial configuration of the Gd-loaded water could be observed, by taking the temperature of the water at different locations in the tank. Figure **??** shows a schematic of the water piping during Gd dissolving for both the inner and outer detectors.
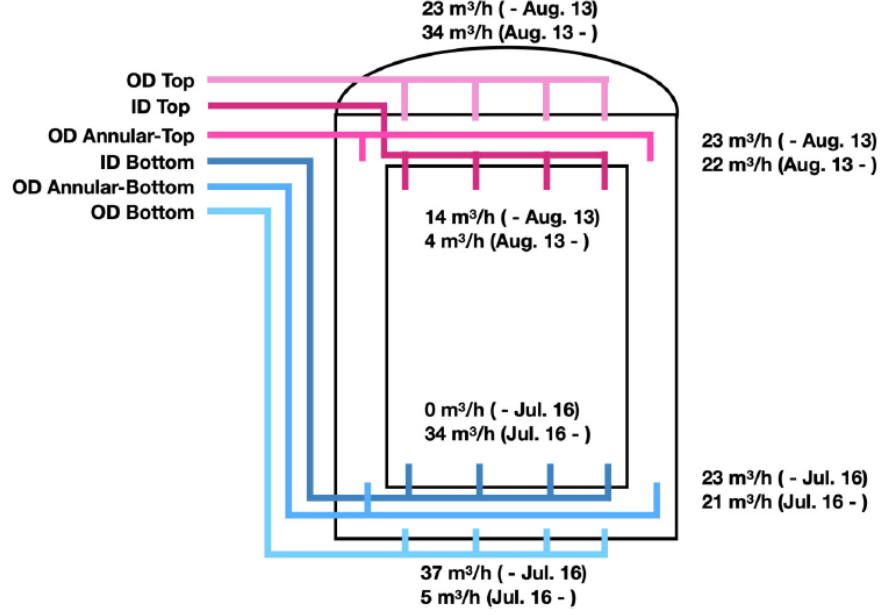
Figure 5.7: Schematic of the SK-Gd water piping for both the ID and OD

Gd-powder specification and loading

The acceptable background rate after the final value for Gd loading (set to be a concentration of 0.1% Gadolinium) was set to be less than double that of the background rate for when Super-Kamioknde ran with pure water. As a result, rigorous standards of cleanliness were set for the

$$\mathrm{Gd_2\left(SO_4\right)_3 \cdot 8H_2O}$$
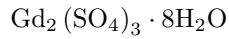
powder, which meant setting maximum allowed levels of radioactive impurites which are shown in Table **??**.

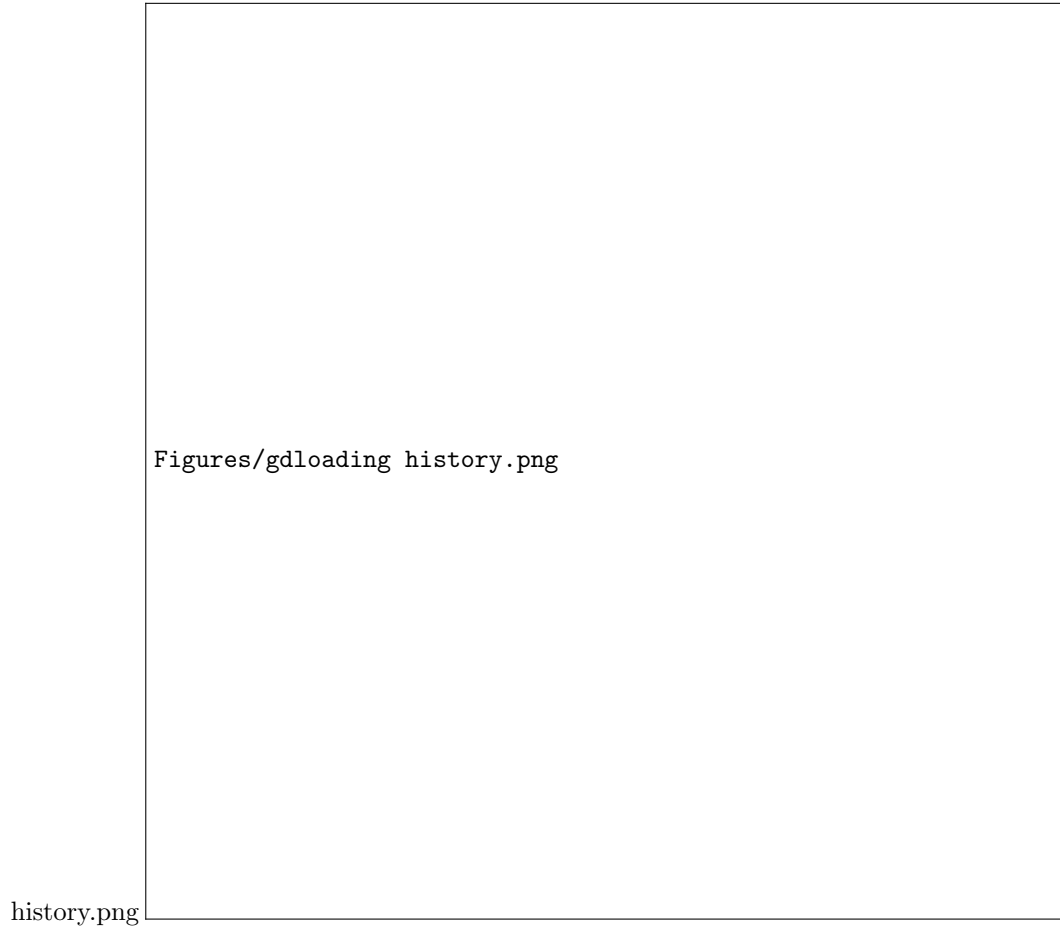| Chain	Isotope	Criterion [mBq/kg]	Physics target
^{238}U	^{238}U	< 5	SRN
	^{226}Ra	< 0.5	Solar
^{232}Th	^{232}Th	< 0.05	Solar
	^{228}Ra	< 0.05	Solar
^{235}U	^{235}U	< 30	Solar
	^{227}Ac/^{227}Th	< 30	Solar

Figures/gdloading history.png

history.png

Figure 5.8: Schematic of the SK-Gd water piping for both the ID and OD

To sustain this very small level of impurity, the gadolinium powder batches went under routine screening at three collaboration laboratories at Boulby (UK), Canfranc (Spain), and the Kamioka Observatory.

Figure ?? shows the loaded mass of gadolinium powder in Super-Kamiokande at each dissolving cycle. The loaded mass of gadolinium sulphade octahydrate powder increased linearly until the target value of 5426 kg of it dissolved in 44,878,429 kg of water in Super-Kamiokande, resulting in a gadolinium concentration of 0.011% and a gadolinium sulphate (

$$Gd_2 \left(SO_4\right)_3$$
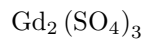
) concentration of 0.021%. After the loading of gadolinium sulphate powder into Super-Kamiokande, water transparency and attenuation length were continously monitored. This had also been conducted in EGADS (see previous section)

23

Chapter 6

Measurement of Neutral Current Quasielastic Interactions with Super-Kamiokande Gadolinium Upgrade

6.1 Bonsai output reconstruction quantities

Due to this analysis looking specifically at the low energy region, a fitter specific to low energies (called LOWFIT) is used to reconstruct events. Both MC and data neutrino events undergo a reconstruction phase, where the low-energy fitter BONSAI is applied to the event, which is discussed in Chapter 2. This reconstruction is carried out using timing and cable information, however charge information is omitted. The ouput of BONSAI gives information which will be used in the reduction phase of the data and allow for the selection of the NCQE sample. The following quantities comprise the BONSAI output, the first two being helpful spectator variables and the latter five constituting parameters which are used in the reduction phase of the analysis, from which the neutrino NCQE sample is determined.

Neutrino vertex direction

This vector points towards the direction which is an average over all the Cherenkov cone axes which are produced, due to there being multiple leptons induced in the interaction.

<u>Neutrino vertex position</u>

The reconstructed location of the neutrino interaction event.

<u>Reconstructed energy</u>

In line with the standard SK low energy analysis definition, this energy is simply the reconstructed energy with the 0.511 MeV electron mass omitted. The range for Erec in this variable is 3.49 MeV to 29.49 MeV - the estimated kinetic energy under the hypothesis that the event is a singular electron.

<u>Dwall</u>

This variable gives the minimum distance of the neutrino vertex position from the closest wall of the Super-Kamiokande detector.

<u>Effwall</u>

Thus variable gives the distance between the neutrino vertex posiiton and the closest wall, but moving back from the vertex position along the neutrino vertex direction vector.

<u>Vertex direction and goodness coefficient</u>

The coefficient $ovaQ$ (defined in Equation **??**) describes the quality of the vertex reconstruction. It consists of two parameters g_{vtx}^2 and g_{dir}^2 where the former describes the goodness of the vertex which is based on PMT hit timings, and increases the sharper an event is in time. The latter is the directional goodness and measures the azimuthal uniformity in the ring pattern produced by the Cherenkov cone, which decreases the more uniform an event is in space. As a result of this, $ovaQ$ increases the more uniform and sharp in time an event is.

$$\text{ova } Q = g_{\text{vtx}}^2 - g_{\text{dir}}^2 \tag{6.1}$$

g_{vtx} is calculated using a fit of the PMT timing distribution and using the hit times of the PMT it is defined asin Equation**??**.

$$g_{\text{vtx}} = \frac{\sum_i w_i e^{-\frac{1}{2}(\frac{\Delta t_i}{\sigma})^2}}{\sum_i w_i} \text{ with } w_i = -\frac{1}{2}(\frac{\Delta t_i}{\omega})^2 \tag{6.2}$$

Here $\sum_i w_i$ is the weight given to the i-th hit PMT for the reduction of dark noise, where ω has a value of 60ns. σ has a value of 5ns which is used to test the goodness, and as a result, a sharp timing distribution produces a large vertex goodness. g_{dir} is calculated by looking at how spatially uniform the hit PMTs are around the reconstructed neutrino vertex direction. In order to quantify this uniformity, the Kolmogorov-Smirnov (KS) test is used as in Equation **??**.

$$g_{\text{dir}} = \frac{\max_i\{\angle_{\text{uni}}(i) - \angle_{\text{data}}(i)\} - \min_i\{\angle_{\text{uni}}(i) - \angle_{\text{data}}(i)\}}{2\pi} \tag{6.3}$$

where $\angle_{\text{data}}(i)$ is the azimuthal angle of i-th hit real PMT included in the number of hits in 50ns. $\angle_{\text{uni}}(i) = 2\pi i/N_{50}$ is the azimuthal angle of the i-th virtual PMT hit, but only when uniform distribution of the hits is assumed. As the uniformity of the hit pattern increases, the goodness decreases.

Cherenkov angle $theta_C$

For relativistic electrons in water, the value of the Cherenkov opening angle is $\approx 41°$, due to the relation:

$$\cos \theta_{\text{Cherenkov}} = \frac{1}{n\beta} \tag{6.4}$$

where $\beta = v/c \approx 1$ and n is the refractive index of water, 1.33. However due to other particles in the simulation, such as protons or muons, the Cherenkov cone is expected to be narrower, or if multiple leptons are present, the Cherenkov cones will be less distinct and more spread out, leading to deviations from the 41°value.

6.1.1   True neutron tagging information

6.1.2   Primary selection criteria

6.1.3   Secondary selection criteria

When the neutron vertex is found by this method, 14 variables which describe different aspects of the neutron candidate are calculated. For each of the neutron candidates the vector of these variables are computed and fed into the neural network and this produces an output value which is between 0 and 1. These variables relate to different features regarding categorising hits from neutron capture on Gd or H, including the number of the hits from neutron capture, the isotropy of these hits, the Cherenkov angles of these hits and the position of the neutron vertex in the detector when capture occurs. A description of these variables are given as follows:

N10nvx

This is the number of hits in the 10ns sliding window of the neutron candidate

N300S

Excluding the number of hits in the 10ns sliding window (N10nvx), this is the number of hits in the extended window of 300ns.

NcS

This variable is defined as:

$$NcS = N10nvx - Nclushit \tag{6.5}$$

Where $Nclushit$ is the number of clusterised hits: if hit i and j are hits on PMTs, then for hit i and hit j the hit vector $\hat{r}_i$ can be written as:

$$\hat{r}_i = \frac{\overrightarrow{PMT_i} - \overrightarrow{VTX_n}}{\left\|\overrightarrow{PMT_i} - \overrightarrow{VTX_n}\right\|} \tag{6.6}$$

where the angle at the point of the neutron capture vertex between $\hat{r}_i$ and $\hat{r}_j$ of the PMT hits is defined as:

$$\theta_{ij} = \arccos\left(\hat{p}_i \cdot \hat{p}_j\right) \tag{6.7}$$

where the hits are defined as clustered if θ_{ij} is less than 14

llrca

This variable is the log likelihood ratio calculated using triplets of hits from N10nvx that make up a rudimentary Cherenkov cone, from which the opening angle θ is calculated. Two PDFs (θ_{Ci}) and (θ_{Ci}) are calculated from each θ_{Ci} where p_s and p_b are the probability density functions of θ_C depending on whether the hits come from a true neutron capture on Gd or H or a false neutron capture which makes up the background. The log likelihood ratio variable is computed using Equation **??**.

$$llrca = \sum_{i \in \{triplets\}} \log\left(\frac{f_B\left(\theta_{Ci}\right)}{f_S\left(\theta_{Ci}\right)}\right) \tag{6.8}$$

beta-n

These variables (where n = 1,2,3,4,5) are defined using Legendre polynomials, shown in Equation **??**, which gives the isotropy of the Cherenkov hits.

$$beta - n = \frac{2}{N10nvx(N10nvx - 1)} \sum_{i \neq j} Legendre_n\left(\cos\theta_{ij}\right) \tag{6.9}$$

where $Legendre_n$ gives the Legendre polynomial of order n and $theta_{ij}$ is the angle between hit PMTs relative to the neutron capture vertex.

ndwall

This parameter, similar to dwall, gives the shortest distance of the neutron capture vertex from the wall of the Super-Kamiokande tank.

ntowall

This variable (similar to effwall), gives the distance of the neutron capture vertex from the wall, however, unlike ndwall it gives the direction of the neutron capture specifically along the direction of the centre of the hits. The direction ($\overrightarrow{R}$) is given by:

$$\overrightarrow{\text{dir}} = \sum_{i=1}^{N10nvx} \hat{p}_i \tag{6.10}$$

Chapter 7

Systematic and statistical uncertainty calculations

7.1 Systematic uncertainty calculation methodology

The systematic uncertainities for this analysis are calculated using the probablity distribution functions of each quantity appearing in the formula for the mean neutron multiplicity, which is given by:

$$M = \frac{\#n_{\mathrm{det}} - R \times \#\nu_{\mathrm{det}}}{T} \frac{1}{\#\nu_{\mathrm{det}}} \qquad (7.1)$$

By random sampling the probability distribution functions for each of the terms in Equation (??) one can calculate the multiplicity probability distribution functions for both the statistical uncertainty and the systematic uncertainty. The statistical uncertainty for the value for the multiplicity is related to the variation in the number of detected neutrons, while the systematic uncertainty is related to the variation on the tagging efficiency and the background rate. The total search time for the tagged neutrons is dependent on the number of "windows" in which the neutron is searched for in, and therefore the term for the number of detected neutrinos. Because any variation on the number of neutrinos which are detected is unrelated to the value for the mean neutron multiplicity, calculating a probability mass function for the number of neutrinos is uneccessary.

A Poissonian distribution is used to model the distribution for the number of detected neutrons, due to its value being approximated by counting the positives in the timing window that the neutron tagging search is carried out in. The mean value of this Poisson distribution is the number of detected neutrons $\langle \#n_{\mathrm{detected}} \rangle$.

$$PMF\left(\#n_{\text{detected}}\right) = \frac{1}{(\#n_{\text{detected}})!} \left\langle \#n_{\text{detected}} \right\rangle^{\#n_{\text{detected}}} e^{-\left\langle \#n_{\text{detected}} \right\rangle} \quad (7.2)$$

Regarding the background rate, this is estimated from dummy spill data. The background rate error is associated with the statistical variation of the Monte Carlo size that the backround rate is associated with, and secondly the change of the background rate value during the SK-V period. The statistical variation of the MC is modelled using a Poisson, but the statistics are high enough so that it appears Gaussian, while the uncertainty relating to time variation is characterised by its own probability distribution function. In contrast, the tagging efficiency is model dependent and has systematic uncertainties relating to this. The two ways in which the systematic error are estimated are either using MC re-weighting or MC regeneration.

For the MC-reweighting approach, weights are applied to a quantity and the tagging efficiency of the re-weighted MC is extracted. The general methodology is to have the input of a model (given by a set of parameters) and to vary them one by one and then calculate the reweighted tagging efficiencies - the set of relative discrepancies δ_i are computed from this set of reweighted tagging efficiencies T_i and the nominal tagging efficiency T_{nom} using Equation (**??**).

$$\delta_i = \frac{T_i - T_{\text{nom}}}{T_{\text{nom}}} \quad i \in \{ \text{ parameters } \} \tag{7.3}$$

These relative discrepancies δ_i are used to calculate the one indivdual discrepancy $\delta_{reweighted}$ that would describe the final deviation from the nominal tagging efficiency T_{nom} due to the systematic error. The parameter $\delta_{reweighted}$ describes the model which has been produced through 1σ variations of these parameters, therefore the final probability distribution function which describes the deviation from the nominal MC has a Gaussian distribution with the standard deviation being equal to $\delta_{reweighted}$.

The other method to estimate the systematic error on the tagging efficiency is the method of Monte Carlo regeneration. This is carried out by varying a parameter then regenerating the whole Monte Carlo and then extracting the tagging efficiency - therefore unlike with MC re-weighting there is no set of discrepancies δ_i but instead two single discrepancies δ_{min} and δ_{max}. The resulting probability distribution which describes the deviation from the nominal Monte Carlo is a Gaussian which has the mean and standard deviation relating to the discrepancies shown in Equation (**??**).

$$\begin{cases} \mu = \frac{\delta_{\text{max}} + \delta_{\text{min}}}{2} \\ \sigma = \frac{\delta_{\text{max}} - \delta_{\text{min}}}{2} \end{cases} \tag{7.4}$$

7.2   Neutrino beam flux uncertainty

The uncertainty on neutrino beam fluxes can be evaluated by looking at the dependence of the tagging efficiency on the flux variations. The beam fluxes for the four flavour modes $(\nu_e \overline{\nu_e} \nu_\mu \overline{\nu_\mu})$ have the fractional uncertainties given for each mode, FHC and RHC. The binned uncertainties are shown in Figure **??**.

Each individual bin for the flux is increased/decreased by its error, the Monte Carlo re-weighting method is then used to extract the tagging efficiency for each flux bin, and Equation (**??**) is used to calculate the fractional uncertainty.

$$\delta_i(\pm\sigma) = \frac{T_i(\pm\sigma) - T_{\text{nom}}}{T_{\text{nom}}} \quad i \in \{ \text{ each flux bin } \} \tag{7.5}$$

Figure **??** shows the fractional errors calculated from the reweighted Monte Carlo, with the red bars showing the -1σ variation and the blue bars showing the +1σ variation. Table **??** contains the value for the total uncertainty resulting from the neutrino beam flux, which was calculated using Equation (**??**), where the maximum value between the increased and decreased discrepancy is taken and summed over to produce the final neutrino flux beam uncertainty.
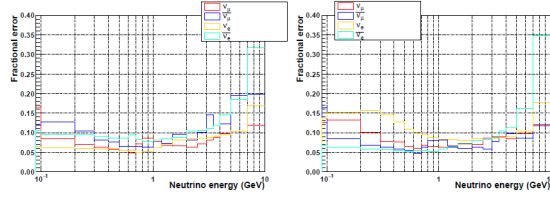

Figure 7.1: Fractional uncertainties of beam fluxes.

$$\delta_{\nu \text{ flux}} = \sum_{i \in \{ \text{ bins } \}} \max \left[|\delta_i(+\sigma)| , |\delta_i(-\sigma)| \right] \tag{7.6}$$
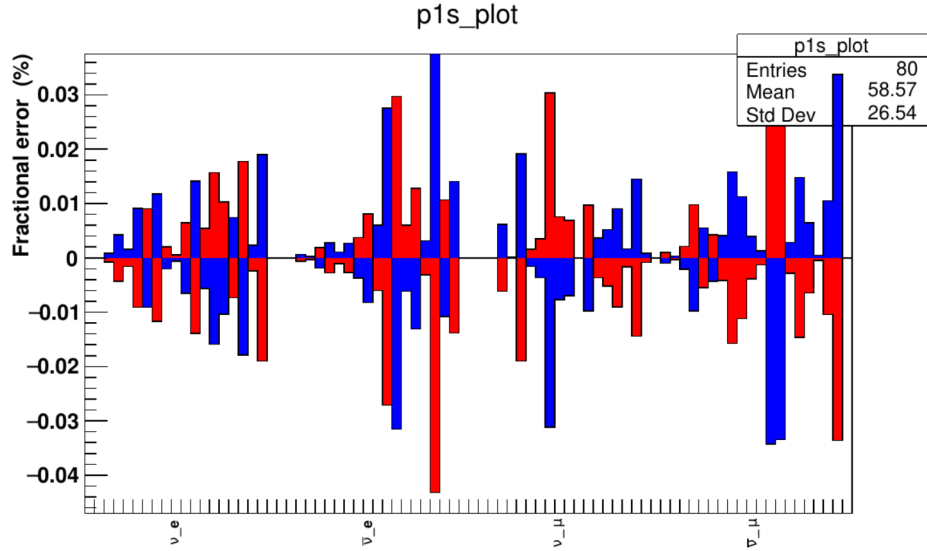
Figure 7.2: Tagging efficiency fractional uncertainties caused by neutrino beam flux discrepancies. From left to right the sections in this plot are comprised of the beam fluxes elements of $(\nu_e \overline{\nu_e} \nu_\mu \overline{\nu_\mu})$ respectively.

7.3 Neutrino cross section uncertainty

A group of default neutrino cross section values are used to make up the nominal Monte Carlo from which the tagging efficiency is calculated. The values of the parameters that determine the cross sections are shown in Table **??**. Each of the parameter values relate to a specific interaction type and are either a normalisation parameter or a paramater which shows a kinematic dependence.

For charged current quasi-elastic interactions, the uncertainty is described by the Fermi momentum of the oxygen nucleus, (p_F^O), the binding energy of the oxygen nucleus,(E_B^O) and the axial mass M_A^{CCQE}. The axial mass for CCQE interactions relates to the axial form factor which along with vector form factors is proportional to the cross section of the interactions. For neutrino interactions where two nucleons produce two holes (2p2h), an overall normalisation parameter takes the uncertainty of these interactions into account. For CC and $NC1\pi$ interactions, the uncertainty is described by the isospin background, the axial form factor C_{A5}^{RES} which just like for CCQE interactions relates to the axial mass M_A^{RES}. For neutral current and charged current interactions (both elastic and inelastic) there are normalisation parameters and energy dependent parameters to take the uncertainty into account. Finally, for charged current interactions with electron neutrinos, the braking radiation from the lepton in the final state is also considered when calculating the uncertainty and is treated using a normalisation parameter.

31

The Monte Carlo re-weighting method is used to reweight the nominal Monte Carlo on an event by event basis with each parameter value being increased and decreased by its uncertainty, and for each reweighted Monte Carlo the equivalent tagging efficiency value is extracted. Equation (**??**) shows how the fractional discrepancies are extracted from the nominal and reweighted tagging efficiency values.

$$\delta_i(\pm\sigma) = \frac{T_i(\pm\sigma) - T_{\text{nom}}}{T_{\text{nom}}} \quad i \in \{ \text{ parameters } \} \tag{7.7}$$

Figure **??** shows the reweighted Monte Carlo fractional uncertainty plotted for the FHC sample. Since this sample contains a lot of NCother interactions, the uncertainty for this interaction type is greater than for the others.

Parameter	Interaction	Type	Value
p_F^O	CCQE	^{16}O Fermi momentum	$225 \pm 31 \text{MeV/c}$
E_B^O	CCQE	^{16}O binding energy	$27 \pm 9 \text{MeV}$
M_A^{CCQE}	CCQE	Axial mass	$1.2 \pm 0.41 \text{GeV/c}^2$
$2p2h$	2p2 h	Normalization par.	1.0 ± 1.0
C_{A5}^{RES}	CC and NC1π	Axial form factor	1.01 ± 0.12
M_A^{RES}	CC and NC1 π	Axial mass	$0.95 \pm 0.15 \text{GeV/c}^2$
BG_A^{RES}	CC and NC1π	I $= 1/2$ continuum background	1.3 ± 0.2
CC other	CC other	E-dependent par.	0.0 ± 0.4
CC elastic	CC elastic	Normalization par.	1.0 ± 0.3
NC other	NC other	E-dependent par.	1.0 ± 0.3
NC elastic	NC elastic	Normalization par.	1.0 ± 0.3
FSe^-Bremsstrahlung	CCν_e	Normalization par.	1.00 ± 0.03

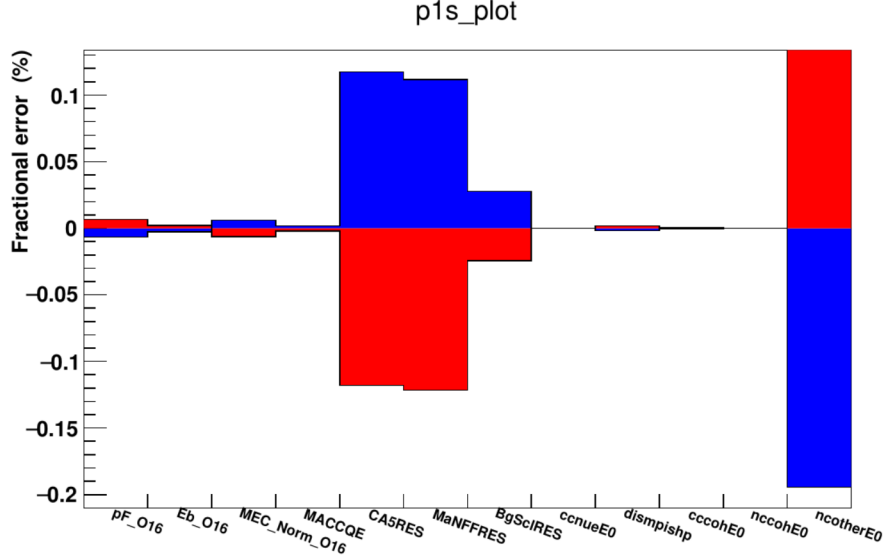Table 7.1: Neutrino cross section parameters

Figure 7.3: Tagging efficiency uncertainty caused by the cross-section parameters variations for the FHC mode

7.4 Pion final state interaction (FSI) and secondary interaction (SI) uncertainties

Even though this is an analysis concerned with neutral current quasi elastic interactions, pion events are a significant contribution to the background, and as a result it is important to examne the pion interaction uncertainties both for final state interactions and secondary interactions as their trajectories span the detector.

The neutrino-nucleus interaction simulator used in this analysis (NEUT) handles pion final state interactions and secondary interactions using a cascade model. This cascade model contains parameters which will have uncertainties on them and these will be tranferred to a possible change in the tagging efficiency.

Depending on the momentum of the pions, different interaction types occur in the model. For pions with a momentum less than 500 MeV, the interactions in place are absorption (ABS), quasi-elastic scattering (QE) and charge exchange (CX)./cite Absorption occurs when the incident pion is absorbed by the nucleus and no pions remain in the final state. Quasi-elastic (QE) scattering occurs when there is only one pion observed in the final state and it has the same charge as the incident beam. Charge exchange occurs when the charged pion interacts wtht he nucleus and a single π_0 can be seen in the final state.

For pions with a momentum of greater than 500 MeV, a different set of interactions are used. Inelastic interactions (INEL) can now produce hadrons

and replace absorption processes, but quasi-elastic scattering (QEH) and charge exchange (CXH) will still occur. The final state interaction parameters and the pion momentum range they are used in can be seen in Table **??**. Each parameter scales the relevant very small proabability of the charged pion interaction at every stage of the intra-nuclear cascade, aside from the parameter for charge exchange which scales only the fraction of low momentum QE scattering.

Parameter	Description	Momentum Region (MeV/c)
f_{ABS}	Absorption	< 500
f_{QE}	Quasi-elastic scatter	< 500
f_{CX}	Single charge exchange	< 500
f_{QEH}	Quasi-elastic scatter	> 500
f_{CXH}	Single charge exchange	> 500
f_{INEL}	Hadron (N + nπ) production	> 500

Table 7.2: Table showing the pion final state interaction parameters in NEUT and the pion momentum range they are used in

A set of paramater variations which determine a surface in paramater space have been estimated by pion scattering experiments, the values for which are shown in Table **??**. The 1σ surface has been explored using the nominal Monte Carlo re-weighting method and the analagous tagging efficiency uncertainty is shown in Equation **??**, and the uncertainty stemming from the models shown in Table **??** is shown in Figure **??**

$$\delta_i = \frac{T_i - T_{\mathrm{nom}}}{T_{\mathrm{nom}}} \quad i \in \text{ parameter vector} \tag{7.8}$$
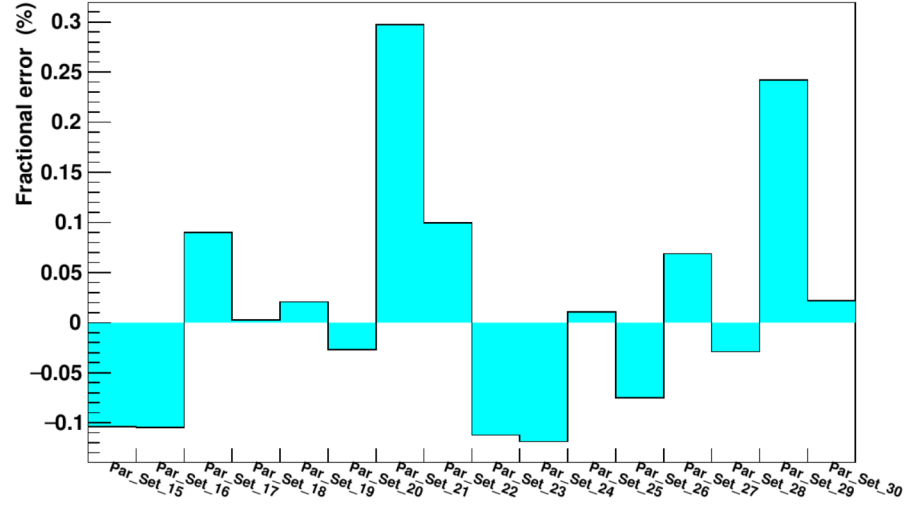
Figure 7.4: Tagging efficiency fractional uncertainty caused by the variation in the FSI/SI model parameters for the FHC mode.

Set	ABS	QE	CX	INEL	QEH	CXH
Nominal	1.1	1.0	1.0	1.0	1.8	1.8
	0.7	0.6	0.5	1.5	1.1	2.3
	0.7	0.6	1.6	1.5	1.1	2.3
Hadron production Up	1.6	0.7	0.4	1.5	1.1	2.3
	1.6	0.7	1.6	1.5	1.1	2.3
	0.6	1.4	0.6	1.5	1.1	2.3
	0.7	1.3	1.6	1.5	1.1	2.3
	1.5	1.5	0.4	1.5	1.1	2.3
	1.6	1.6	1.6	1.5	1.1	2.3
	0.7	0.6	0.5	0.5	2.3	1.3
	0.7	0.6	1.6	0.5	2.3	1.3
	1.6	0.7	0.4	0.5	2.3	1.3
Hadron production Down	1.6	0.7	1.6	0.5	2.3	1.3
	0.6	1.4	0.6	0.5	2.3	1.3
	0.7	1.3	1.6	0.5	2.3	1.3
	1.5	1.5	0.4	0.5	2.3	1.3
	1.6	1.6	1.6	0.5	2.3	1.3

Table 7.3: Pion FSI/SI model parameter nominal value and variations grouped according to inelastic hadron production value

7.5 Nucleon final state interactions

Uncertainties regarding the nucleon final state interactions can change the number of nucleons knocked out of ^{16}O, therefore how the tagging efficiency is changed due to the variation in nucleon final state interactions needs to be investigated. This uncertainty is extracted using GENIE, a Monte Carlo event generator which contains the INTRANUKE (hA) intranuclear transport model. The uncertainties in the in the total scattering probability for hadrons inside the target nuclei (x_{mfp}^N) and the uncertainties in the likelihood of each hadron rescattering method: (elastic (x_{el}^N), inelastic (x_{inel}^N), charge exchange (x_{cex}^N), pion production (x_π^N) and absorption (x_{abs}^N)) are taken into account. The fractional uncertainties for these modes for pions is shown in Table **??**.

Abbreviation	Description of uncertainty	Fractional uncertainty
x^N_{mfp}	Nucleon mean free path (total rescattering probability)	$\pm 20\%$
x^N_{cex}	Nucleon charge exchange probability	$\pm 50\%$
x^N_{el}	Nucleon elastic reaction probability	$\pm 30\%$
x^N_{inel}	Nucleon inelastic reaction probability	$\pm 40\%$
x^N_{abs}	Nucleon absorption probability	$\pm 20\%$
x^N_{π}	Nucleon π-production probability	$\pm 20\%$

Table 7.4: Nucleon final state interaction parameters of the hA model executed inside GENIE.

A nominal GENIE Monte Carlo sample is generated (different from the previously used NEUT Monte Carlo) and this shifted using the re-weighting method to a varied GENIE Monte Carlo by individually increasing and decreasing the parameters in Table **??** by its error. For each shifted Monte Carlo produced, the fractional uncertainty can be written as in Equation **??**.

$$\delta_i(\pm\sigma) = \frac{T_i(\pm\sigma) - T_{\text{nom}}}{T_{\text{nom}}} \quad i \in \{ \text{ parameters } \} \tag{7.9}$$

The tagging efficiency fractional uncertainties are displayed in Figure **??**, showing which parameter from Table **??** each uncertainty has arisen from.
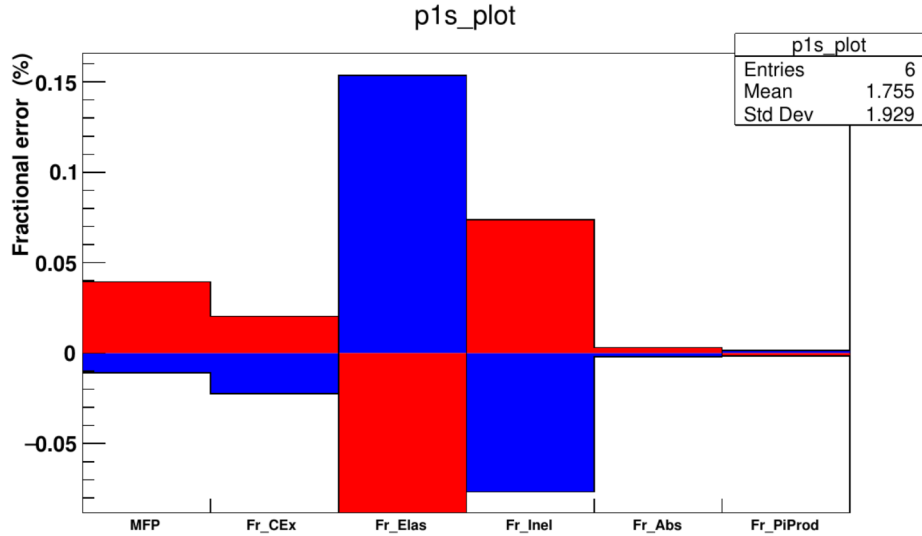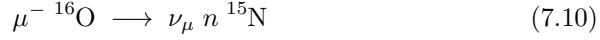

Figure 7.5: Tagging efficiency fractional uncertainties caused by the nucleon final state interaction model parameter variation for the FHC mode

7.6 Muon and pion capture on ^{16}O

Neutrons are produced from negative muon capture on ^{16}O as show in Equation **??**.

$$\mu^- \; {}^{16}\text{O} \; \longrightarrow \; \nu_\mu \; n \; {}^{15}\text{N} \tag{7.10}$$

Direct neutrons are produced from pion capture on ^{16}O, but also a number of evaporation neutrons that leave the nucleus. For the capture of muons and pions on ^{16}O, the energy spectra of the neutrons produced have been measured: for muons the spectra can range up to 15 MeV, while in the case of pions the spectra can reach up to 100 MeV.

Geant4 simulates the capture processes for muons and pions, but there are alternate models that can be used: for example, the Chiral Invariant Phase Space (CHIPS) model for muon captures (based on non pertubative QCD) and two different routines for pion capture, one which is based on CHIPS and one based on intra-nuclear cascade.

Because any change in the model can alter the energy spectra of the neutrons, these alternative functions can be used to estimate the fractional uncertainties for the tagging efficiency. This is done by using the MC regeneration method, where the nominal Monte Carlo is regenerated by replacing the default Geant4 routines with the alternative models. For the alterantive muon capture model and the two alternative pion capture models, the fractional discrepancies are shown in Equation **??**.

$$\begin{aligned}
\delta_{muonCHIPS} &= \frac{T_{muonCHIPS} - T_{nom}}{T_{\text{nom}}} \\
\delta_{pionCHIPS} &= \frac{T_{pionCHIPS} - T_{nom}}{T_{\text{nom}}} \\
\delta_{pionBert} &= \frac{T_{pionBert} - T_{nom}}{T_{\text{nom}}}
\end{aligned} \tag{7.11}$$

Chapter 8

Conclusion